

©2008 IEEE. Personal use of this material is permitted. However, permission to reprint/republish this material for advertising or promotional purposes or for creating new collective works for resale or redistribution to servers or lists, or to reuse any copyrighted component of this work in other works must be obtained from the IEEE.

Ionospheric Error Modeling for Carrier Phase-Based Multi-Constellation Navigation Systems

Mathieu Joerger, *Member, IEEE*, Jason Neale, Seebany Datta-Barua and Boris Pervan, *Member, IEEE*

Abstract— This paper describes the design, analysis and evaluation of new ionospheric measurement error models for high-integrity multi-constellation navigation systems. The robustness of the newly-derived models is experimentally evaluated using months of dual-frequency GPS data collected at multiple locations. In parallel, an integrity analysis is devised to quantify the impact of traveling ionospheric disturbances on user position. Finally, overall carrier-phase positioning performance is assessed over continental areas, for various combinations of GPS, Galileo and Iridium satellites.

Index Terms — robust modeling, traveling ionospheric disturbance (TID), fault detection, multi-constellation

I. INTRODUCTION

The integration of ranging signals from multiple satellite constellations opens the possibility for rapid, robust and accurate positioning over wide areas. In this paper, robust measurement error models are established to enable precise non-differential navigation using low-broadcast-rate wide-area corrections. These models are incorporated in algorithms that exploit multi-constellation signal redundancy and geometric diversity to perform rapid floating carrier phase cycle ambiguity estimation, and fault-detection using carrier phase Receiver

Manuscript received December 6, 2010. The authors gratefully acknowledge The Boeing Co. and the Naval Research Laboratory for sponsoring this work. However, the opinions expressed in this paper do not necessarily represent those of any other organization or person.

M. Joerger, and B. Pervan are with the Illinois Institute of Technology, Chicago, IL 60616 USA (phone: 312-567-8863; fax: 312-567-7230; e-mail: joeremat@iit.edu).

J. Neale is with L3 Communications, Hollywood, MD 20636 USA.

S. Datta-Barua is with San Jose State University, San Jose, CA 95192 USA.

Autonomous Integrity Monitoring (RAIM). An overall system integrity analysis is devised and implemented. The analysis explores the potential of multi-constellation navigation systems to provide robust carrier phase positioning at continental scales.

Carrier phase positioning is contingent upon estimation (or resolution) of cycle ambiguities. These remain constant as long as satellite signals are continuously tracked by the receiver. An efficient solution for cycle ambiguity estimation is to use the bias observability provided by redundant satellite motion [1]. This principle was demonstrated in [2] to be particularly effective in navigation systems that augment GPS with ranging signals from fast moving low earth orbit (LEO) spacecraft.

Estimation and detection algorithms were designed in [3] to fully exploit angular variations in satellite lines of sight (LOS). A fixed-interval smoother was established for combined estimation of user position and floating cycle ambiguities. Fault-detection was achieved using a batch least-squares residual-based RAIM method. The algorithms were evaluated with sequences of code and carrier phase measurements from GPS and from LEO Iridium telecommunication space vehicles (SV).

However, one major challenge in validating these algorithms for high-integrity precision applications is ensuring the robustness of measurement error models. Time-processing (needed for cycle ambiguity estimation) introduces an additional dimension to the problem in that the dynamics over time of the errors and faults must be carefully accounted for. In reference [4], a nominal configuration for a notional near-future LEO satellite-augmented GPS navigation system was assumed, for single-frequency users receiving low-rate corrections from a network of wide-area ground stations (e.g., similar to the Wide Area Augmentation System or WAAS). The resulting measurement equation expressed measurement dependency on error sources including satellite clock and orbit ephemeris, ionospheric and tropospheric refraction, multipath and receiver noise. For single-frequency implementations using wide-area differential corrections, the ionosphere is the most influential source of error.

In this work, the nominal ionospheric error model derived in [4] is evaluated against months

of experimental data collected at multiple Continuously Operating Reference Stations (CORS). The analysis shows that a piecewise linear model of the vertical ionospheric delay captures most of the ionospheric variations at mid-latitudes. However, the ionosphere also exhibits localized wave-like structures causing decimeter-level errors on low-elevation SV signals. These structures are often referred to as Traveling Ionospheric Disturbances (TIDs) [5]. The amplitude of TIDs is an order of magnitude larger than the carrier phase tracking noise, which is why their impact on ranging measurements must be accounted for in high-integrity carrier phase navigation applications.

In response, in this research, two new strategies are devised. The first one is to derive a new measurement error model that accounts for sinusoidal error variations due to TIDs. The fidelity of the model to the data is quantified by establishing the probability distribution of residual errors obtained after removing the estimated ionospheric delay from the data. If the resulting residual errors are still large relative to the carrier tracking noise, then the second strategy can be employed. The second approach, which is used here to complement the nominal error model, is a conservative error-bounding procedure to include mis-modeling errors with unknown time-behavior in the estimation and detection algorithms. Parameters of the error models and of the bounding approach are determined using experimental data, as well as values cited in the literature. They are implemented to predict and analyze the performance of carrier-phase based multi-constellation navigation systems under non-stormy ionospheric conditions.

Performance evaluations are structured around benchmark requirements inspired from civilian aviation standards. An example application of aircraft precision approach is considered. Fault-free (FF) integrity is evaluated by covariance analysis, and RAIM detection performance is quantified for a set of step and ramp-type single-satellite faults (SSF) of all magnitudes and starting times. A sensitivity analysis of the combined FF and SSF performance assesses the influence of new parameters in the updated ionospheric error model. In particular, it reveals the decisive impact of TIDs on user positioning performance.

Section II of this paper summarizes the background on carrier phase-based position estimation

and detection algorithms. Mis-modeling errors are incorporated in these algorithms using the approach presented in Sec. III. In Sec. IV and V, ionospheric error models are defined and evaluated based on experimental data from CORS. The overall system performance is established in Sec. VI for near future single-frequency implementations and for longer-term future, dual-frequency, multi-constellation navigation systems including combined GPS/Galileo, Iridium/GPS and Iridium/GPS/Galileo constellations. Section VII contains concluding remarks.

II. BACKGROUND ON ESTIMATION AND DETECTION ALGORITHMS

A. Complete Measurement Equation

A fixed-interval smoothing algorithm was devised in [3] for the simultaneous estimation of user position and of floating carrier phase cycle ambiguities from carrier phase and code observations. Under nominal FF conditions the linearized carrier phase observation for a satellite s at epoch k is expressed as:

$$\begin{aligned} {}^s\phi_k = & {}^s\mathbf{g}_k^T \mathbf{u}_k + {}^sN - {}^s\mathcal{E}_{I,k} + {}^s\mathcal{E}_{SVOC,k} \\ & + {}^s\mathcal{E}_{T,k} + {}^s\mathcal{E}_{M,\phi,k} + {}^sV_{RN,\phi,k} \end{aligned} \quad (1)$$

where:

\mathbf{u}_k is the vector of user position (e.g., in a local reference frame) and receiver clock bias,

${}^s\mathbf{g}_k^T = [{}^s\mathbf{e}_k^T \ 1]$ and ${}^s\mathbf{e}_k^T$ is the unit LOS vector,

sN is the carrier phase cycle ambiguity,

${}^s\mathcal{E}_{I,k}$ is the ionospheric error

${}^s\mathcal{E}_{SVOC,k}$ is the satellite orbit ephemeris and clock error

${}^s\mathcal{E}_{T,k}$ is the residual tropospheric delay

and ${}^sV_{RN,\phi,k}$ and ${}^s\mathcal{E}_{M,\phi,k}$ respectively are the carrier phase receiver noise and multipath error.

Nominal measurement error models for ${}^s\mathcal{E}_{I,k}$, ${}^s\mathcal{E}_{SVOC,k}$ and ${}^s\mathcal{E}_{T,k}$ are described in detail in [3].

For example, it is assumed that over a short smoothing interval T_F (of 10 min or less), the satellite orbit ephemeris and clock error ${}^s\varepsilon_{SIOC,k}$ can be modeled as a bias ${}^sb_{SIOC}$ plus a ramp over time of constant slope ${}^sg_{SIOC}$. The nominal model for ${}^s\varepsilon_{I,k}$ is revisited in Sec. IV. Also, ${}^sv_{RN,\phi,k}$ is modeled as a zero-mean Gaussian white noise sequence with variance $\sigma_{RN,\phi}^2$ (we use the notation $v_{RN,\phi,k} \sim \mathbf{N}(0, \sigma_{RN,\phi}^2)$). The term ${}^s\varepsilon_{M,\phi,k}$ is modeled as a first-order Gauss-Markov process with time constant T_M , variance $\sigma_{M,\phi}^2$ and driving noise $v_{M,\phi,k}$.

The equation for the linearized code phase measurement ${}^s\rho_k$ is identical to (1) except for the absence of the cycle ambiguity bias sN and a positive sign on the ionospheric error ${}^s\varepsilon_{I,k}$. Also, the carrier phase receiver noise ${}^sv_{RN,\phi,k}$ and multipath error ${}^s\varepsilon_{M,\phi,k}$ are respectively replaced by the code receiver noise ${}^sv_{RN,\rho,k}$ (with $v_{RN,\rho,k} \sim \mathbf{N}(0, \sigma_{RN,\rho}^2)$) and multipath term ${}^s\varepsilon_{M,\rho,k}$ (with $v_{M,\rho,k} \sim \mathbf{N}(0, \sigma_{\rho,\phi}^2(1 - e^{-2T_{SB}/T_M}))$).

B. Fixed-Interval Estimation Algorithm

The fixed-interval smoothing algorithm is suitable for real-time implementation provided that sufficient memory is allocated to the storage of a finite number of past measurements and LOS coefficients collected over a smoothing period T_F . Current-time (and past-time) optimal state estimates are obtained from iteratively feeding the stored finite sequence of observations into a forward-backward smoother. Past-time estimates are used in the RAIM-based procedure for residual generation. The smoother is equivalent to a batch measurement processing method, which is summarized below. For the complete derivation, see [3].

The complete sequence of code and carrier phase signals for all n_s visible satellites over n_p time epochs (included in the smoothing interval T_F) are stacked in a batch measurement vector \mathbf{z} that can be expressed as a state space realization:

$$\mathbf{z} = \mathbf{H}\mathbf{x} + \mathbf{v}, \quad (2)$$

where the state vector is:

$$\mathbf{x} = \left[\mathbf{u}_1^T \quad \mathbf{L} \quad \mathbf{u}_k^T \quad \mathbf{L} \quad \mathbf{u}_{n_p}^T \quad \mathbf{N}^T \quad \mathbf{x}_{ERR}^T \right]^T. \quad (3)$$

The dynamics of the user position and receiver clock deviation vector \mathbf{u}_k are unknown. Different states are therefore allocated for the 4×1 vector \mathbf{u}_k at each time step k (ranging from epoch 1 to n_p), as opposed to the other parameters that are modeled as constants over interval T_F . The vector \mathbf{N} is comprised of cycle ambiguity states for all satellites ($\mathbf{N} = [{}^1N \quad \mathbf{L} \quad {}^{n_s}N]^T$). State augmentation is used to incorporate the dynamics of the measurement error models. Thus, the error state vector \mathbf{x}_{ERR} in (3) is made of constant parameters of the error models (e.g., bias ${}^s b_{SVO C}$ and gradient ${}^s g_{SVO C}$ parameters for satellite-related faults). A detailed description of \mathbf{x}_{ERR} is given in Appendix I and is not needed for the next steps of the algorithm derivation. Finally, the measurement noise vector \mathbf{v} in (2), with covariance matrix \mathbf{V} , is utilized to introduce the time-correlated noise due to multipath as well as receiver noise. Detailed derivations of the measurement covariance matrix \mathbf{V} and observation matrix \mathbf{H} , which includes error state coefficients, are given in [3].

The weighted least squares state estimate $\hat{\mathbf{x}}$ (with covariance matrix \mathbf{P}_x) includes prior knowledge (subscript PK) on a subset of states and is obtained using the weighted pseudo-inverse \mathbf{S} of \mathbf{H} :

$$\hat{\mathbf{x}} = \underbrace{\mathbf{D} \mathbf{H}^T \mathbf{V}^{-1}}_{\mathbf{S}} \mathbf{z} \quad (4)$$

where

$$\mathbf{P}_x = \left(\begin{bmatrix} \mathbf{0} & \mathbf{0} \\ \mathbf{0} & \mathbf{P}_{PK}^{-1} \end{bmatrix} + \mathbf{H}^T \mathbf{V}^{-1} \mathbf{H} \right)^{-1}.$$

Prior knowledge on the error state vector \mathbf{x}_{ERR} is expressed in terms of bounding values on each element's probability distributions, and included in the system with the a-priori information matrix \mathbf{P}_{PK}^{-1} (defined in Appendix I).

If the focus of the estimation performance analysis is on a subset of states, for example on the current-time vertical position state x_U , a transformation matrix \mathbf{T}_U can be defined to select that

element, as:

$$\mathbf{T}_U = \begin{bmatrix} \mathbf{0}_{1 \times n_A} & 1 & \mathbf{0}_{1 \times n_B} \end{bmatrix} \quad (5)$$

where n_A and n_B are the numbers of states respectively before and after x_U (so that $n_x = n_A + 1 + n_B$). The diagonal element of \mathbf{P}_x corresponding to the current-time vertical position covariance is noted σ_U^2 and can be expressed as:

$$\sigma_U^2 = \mathbf{T}_U \mathbf{P}_x \mathbf{T}_U^T. \quad (6)$$

The standard deviation σ_U is used in Appendix II to determine FF availability.

C. Batch Residual RAIM Detection Algorithm

State estimation is based on a history of observations, all of which are vulnerable to satellite faults. To protect the system against abnormal events, a RAIM-type process is implemented, using the least-squares residuals of the batch measurement equation (2). The least-squares residual RAIM methodology [6] gives a statistical description of the impact of a measurement fault vector \mathbf{f} (of same dimension as \mathbf{z}), whose non-zero elements introduce deviations from normal FF conditions. Equation (2) becomes:

$$\mathbf{z} = \mathbf{H}\mathbf{x} + \mathbf{v} + \mathbf{f}, \quad (7)$$

The residual-based RAIM methodology investigates the impact of the fault vector \mathbf{f}

- on the current-time vertical position state estimate error δx_U :

$$\delta x_U \equiv x_U - \hat{x}_U = \mathbf{T}_U \mathbf{S}(\mathbf{v} + \mathbf{f}) \quad (8)$$

$$\delta x_U \sim N(\mathbf{T}_U \mathbf{S} \mathbf{f}, \sigma_U^2). \quad (9)$$

- and on a test statistic derived from the batch least-squares residual vector \mathbf{r} :

$$\mathbf{r} \equiv (\mathbf{I} - \mathbf{H}\mathbf{S})\mathbf{z} = (\mathbf{I} - \mathbf{H}\mathbf{S})(\mathbf{v} + \mathbf{f}), \quad (10)$$

where \mathbf{I} is the identity matrix of appropriate size. The test statistic is the weighted norm

of \mathbf{r} (defined as $\|\mathbf{r}\|_w^2 = \mathbf{r}^T \mathbf{V}^{-1} \mathbf{r}$). It follows a non-central chi-square distribution with $n_z - (4n_p + n_s)$ degrees of freedom (n_z is the number of measurements) and non-centrality parameter λ_{SSF}^2 (which can be expressed as $\lambda_{SSF}^2 = \mathbf{f}^T \mathbf{V}^{-1} (\mathbf{I} - \mathbf{H}\mathbf{S}) \mathbf{f}$) [7].

The probability of missed detection P_{MD} is then defined as a joint probability:

$$P_{MD} = P\left(|\delta x_U| > VAL, \|\mathbf{r}\|_w < R_C \right). \quad (11)$$

where VAL is a vertical alert limit, and R_C is a detection threshold set to limit the probability of false alarms under fault free conditions [8]. The probability P_{MD} is used in Appendix II to determine SSF availability.

III. CONSERVATIVE APPROACH TO ACCOUNT FOR MIS-MODELING ERRORS DUE TO TIDS

Measurement error models must account for the instantaneous uncertainty at smoother initiation (absolute measurement error) as well as error variations over the smoothing duration (relative error with respect to initialization). Data from CORS are processed in Sec. V to quantify the residual ionospheric error after differencing the model from the experimental data. Maximum observed values of residual errors due to TIDs can be measured, but their time-behavior is extremely difficult to model. Also, TIDs are shown to occur too frequently to be considered rare-event faults. Therefore, in this subsection, a conservative approach is taken to evaluate the impact of mis-modeling errors caused by TIDs on FF estimation and on detection performance.

A mis-modeling error vector $\boldsymbol{\varepsilon}$ is added to the FF measurement equation (2):

$$\mathbf{z} = \mathbf{H}\mathbf{x} + \mathbf{v} + \boldsymbol{\varepsilon} \quad (12)$$

Mis-modeling errors caused by TIDs, which are localized, temporary phenomena, affect a subset of measurements. In most cases observed in Sec. V, TIDs impact measurements from a single satellite. However, cases of multiple signals being simultaneously affected are also considered because they are more likely to occur in a multi-constellation architecture. A transformation matrix \mathbf{T}_{ZS} can be employed to isolate non-zero elements of $\boldsymbol{\varepsilon}$. For example, for

single-satellite errors affecting the n_{ZS} observations of a satellite s , the $n_Z \times n_{ZS}$ matrix \mathbf{T}_{ZS} is defined as:

$$\mathbf{T}_{ZS} = [\mathbf{0}_{n_{ZS} \times n_{ZA}} \quad \mathbf{I}_{n_{ZS}} \quad \mathbf{0}_{n_{ZS} \times n_{ZB}}]^T, \quad (13)$$

where, following the order in which measurements are stacked in \mathbf{z} , n_{ZA} and n_{ZB} are the numbers of measurements respectively before and after measurements from satellite s ($n_Z = n_{ZA} + n_{ZS} + n_{ZB}$). The satellite whose observations have the largest impact on the states of interest (e.g., on the current-time vertical position coordinate) can be selected using the following criterion:

$$\max_s \left(\mathbf{T}_{ZS}^T \mathbf{S}^T \mathbf{T}_U^T \mathbf{T}_{ZS} \mathbf{S} \right). \quad (14)$$

A similar method is implemented to account for the impact of TIDs on multiple satellite signals. In the worst theoretical case where all observations are impacted (which is unlikely to occur but is included for the analysis), \mathbf{T}_{ZS} is the $n_Z \times n_Z$ identity matrix (and $n_{ZS} = n_Z$).

Let $\boldsymbol{\varepsilon}_{TID}$ be the $n_{ZS} \times 1$ vector of (non-zero) residual ranging errors due to TIDs. The FF measurement equation (12) becomes

$$\mathbf{z} = \mathbf{H}\mathbf{x} + \mathbf{v} + \mathbf{T}_{ZS}\boldsymbol{\varepsilon}_{TID}. \quad (15)$$

An upper limit b is established for the impact of $\boldsymbol{\varepsilon}_{TID}$ on the states of interest (e.g., on the current-time vertical position estimate x_U) using Hölder's inequality [9]:

$$|\mathbf{T}_U \mathbf{S} \mathbf{T}_{ZS} \boldsymbol{\varepsilon}_{TID}| \leq \|\mathbf{T}_U \mathbf{S} \mathbf{T}_{ZS}\|_1 \|\boldsymbol{\varepsilon}_{TID}\|_\infty \quad (16)$$

where

$$\|\boldsymbol{\varepsilon}_{TID}\|_\infty = \max \left(|\boldsymbol{\varepsilon}_{TID,1}|, |\boldsymbol{\varepsilon}_{TID,2}|, \dots, |\boldsymbol{\varepsilon}_{TID,n_{ZS}}| \right), \quad (17)$$

$$\|\mathbf{T}_U \mathbf{S} \mathbf{T}_{ZS}\|_1 = \sum_{i=1}^{n_{ZS}} |(\mathbf{T}_U \mathbf{S} \mathbf{T}_{ZS})_i|, \quad (18)$$

and $(\mathbf{T}_U \mathbf{S} \mathbf{T}_{ZS})_i$ is the i^{th} element of the $1 \times n_{ZS}$ row vector $\mathbf{T}_U \mathbf{S} \mathbf{T}_{ZS}$. The maximum value that any element of $\boldsymbol{\varepsilon}_{TID}$ can take is noted:

$$\|\boldsymbol{\varepsilon}_{TID}\|_\infty = \beta_{TID}. \quad (19)$$

The upper bound b of the impact of $\boldsymbol{\varepsilon}_{TID}$ on x_U is expressed as:

$$b = \beta_{TID} \sum_{i=1}^{n_{ZS}} |(\mathbf{T}_U \mathbf{S} \mathbf{T}_{ZS})_i|. \quad (20)$$

It is used in Appendix II to establish a conservative FF performance criterion in the presence of mis-modeling errors.

In addition, for the SSF performance analysis, the mean of the estimate error δx_U in (9) is modified to:

$$\delta x_U \sim \mathcal{N}(\mathbf{T}_U \mathbf{S} \mathbf{f} + b, \sigma_U^2). \quad (21)$$

The vector $\boldsymbol{\varepsilon}_{TID}$ in (15) also causes the detection threshold R_C to become non-centrally chi-square distributed. The fault-free non-centrality parameter λ_{FF}^2 is defined as:

$$\lambda_{FF}^2 = \boldsymbol{\varepsilon}_{TID}^T \mathbf{T}_{ZS}^T \mathbf{V}^{-1} (\mathbf{I} - \mathbf{H} \mathbf{S}) \mathbf{T}_{ZS} \boldsymbol{\varepsilon}_{TID}. \quad (22)$$

Let v_{MAX}^2 be the largest eigenvalue of the symmetric matrix $\mathbf{T}_{ZS}^T \mathbf{V}^{-1} (\mathbf{I} - \mathbf{H} \mathbf{S}) \mathbf{T}_{ZS}$, and let \mathbf{v}_{MAX} be the corresponding eigenvector (i.e., the unit vector of the TID profile over time, which maximizes λ_{FF}^2). A conservative value for the non-centrality parameter λ_{FF}^2 of R_C is:

$$\lambda_{FF,MAX}^2 = \beta_{TID}^2 v_{MAX}^2 / \|\mathbf{v}_{MAX}\|_{\infty}^2. \quad (23)$$

The final step of this conservative approach is to minimize the impact of $\boldsymbol{\varepsilon}_{TID}$ on the residual \mathbf{r} . The non-centrality parameter λ_{SSF}^2 of $\|\mathbf{r}\|_W^2$ becomes:

$$\lambda_{SSF}^2 = (\mathbf{f} + \mathbf{T}_{ZS} \boldsymbol{\varepsilon}_{TID})^T \mathbf{V}^{-1} (\mathbf{I} - \mathbf{H} \mathbf{S}) (\mathbf{f} + \mathbf{T}_{ZS} \boldsymbol{\varepsilon}_{TID}) \quad (24)$$

The parameter λ_{SSF}^2 is the squared norm of the vector $(\mathbf{f} + \mathbf{T}_{ZS} \boldsymbol{\varepsilon}_{TID})$ weighted by the matrix $\mathbf{V}^{-1} (\mathbf{I} - \mathbf{H} \mathbf{S})$. A lower limit on this norm is the difference between the weighted norms of \mathbf{f} and $\mathbf{T}_{ZS} \boldsymbol{\varepsilon}_{TID}$, so that:

$$\lambda_{SSF} \geq \sqrt{\mathbf{f}^T \mathbf{V}^{-1} (\mathbf{I} - \mathbf{H} \mathbf{S}) \mathbf{f}} - \sqrt{\boldsymbol{\varepsilon}_{TID}^T \mathbf{T}_{ZS}^T \mathbf{V}^{-1} (\mathbf{I} - \mathbf{H} \mathbf{S}) \mathbf{T}_{ZS} \boldsymbol{\varepsilon}_{TID}}. \quad (25)$$

An upper bound on the term $\boldsymbol{\varepsilon}_{TID}^T \mathbf{T}_{ZS}^T \mathbf{V}^{-1} (\mathbf{I} - \mathbf{H} \mathbf{S}) \mathbf{T}_{ZS} \boldsymbol{\varepsilon}_{TID}$ was computed in (23), so that (25)

becomes:

$$\lambda_{SSF} \geq \sqrt{\mathbf{f}^T \mathbf{V}^{-1} (\mathbf{I} - \mathbf{H}\mathbf{S}) \mathbf{f}} - \lambda_{FF,MAX}. \quad (26)$$

Therefore, a conservative value for the residual's non-centrality parameter is:

$$\lambda_{SSF,MIN} = \sqrt{\mathbf{f}^T \mathbf{V}^{-1} (\mathbf{I} - \mathbf{H}\mathbf{S}) \mathbf{f}} - \lambda_{FF,MAX}. \quad (27)$$

Equations (21), (23) and (27) are used in Appendix II to compute the probability P_{MD} and hence, to evaluate the SSF performance in the presence of mis-modeling errors.

IV. IONOSPHERIC ERROR MODELS

Ionospheric errors affecting satellite ranging measurements can be effectively eliminated using dual-frequency signals or differential corrections from nearby reference stations. In this work, an attempt is made at fulfilling stringent integrity requirements using a non-differential single-frequency navigation system configuration. To achieve this objective, reference [4] introduced a nominal measurement error model of single-frequency signals from both GPS and LEO satellites, which is refined in this section.

A. Properties of Traveling Ionospheric Disturbances (TIDs)

The motivation for designing a new ionospheric error model stems from observations of experimental data. Fig. 1 is a preview of ionospheric delay measurements processed and analyzed in Sec. V. These measurements are derived from dual-frequency GPS carrier phase data collected at the Battle Creek, Michigan CORS reference station on January 8, 2007, which was a day of quiet ionospheric activity (A_K index of 2 [10]). Between 2:26 pm and 2:48 pm local time, the PRN 13 satellite elevation angle was increasing between 10 deg and 14 deg. Over this 22 min-long time span, the raypath of the satellite signal travelled a distance d_{IPP} of 700 km across the ionosphere, at the height h_f of 350 km where the highest electron density is assumed (d_{IPP} computations are explained in Sec IV-B). The upper graph displays both the measured ionospheric error (thick line) and the error estimated using a piecewise linear model of the vertical ionospheric delay described in Sec. IV-B (thin dashed line). This error model is used to

detrend the data in the lower graph (obtained by differencing the thick and thin lines of the upper plot). The piecewise linear model accounts for the largest part of the ionospheric delay (at the several-meter level), but substantial residual mis-modeling errors remain. The residuals are at the decimeter level, which is an order of magnitude larger than carrier phase tracking noise. These residual errors must be accounted for to ensure the integrity of the non-differential, single-frequency carrier phase-based navigation system.

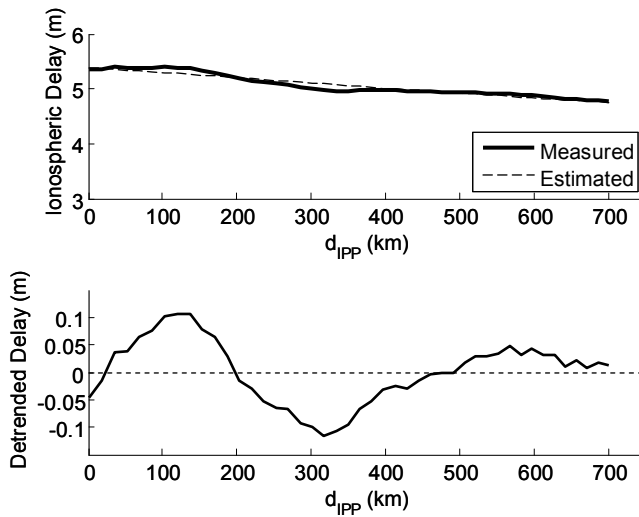


Fig. 1. Wave-Like Structure Observed in Ionospheric Delay Measurements

The wave-like structure observed in Fig. 1 is actually a travelling ionospheric disturbance (TID). Evidence corroborating this statement is provided in Sec V-D with an experimental analysis of the ionosphere for data collected over several months at multiple locations.

TIDs are quasi-periodic propagating ionospheric disturbances. As a subject of research over several decades, they have been observed at all latitudes, longitudes, times of day, season, and solar cycle [11, 12]. They are generally thought to be caused by the propagation of atmospheric gravity waves through the neutral atmosphere, which in turn perturbs the ionospheric electron density distribution.

Typical values for the velocity, wavelength and amplitude of medium-scale TIDs are

respectively 50-300 m/s [13, 14], 100-300 km [5, 15, 16], and up to 3.5 total electron content units (TECU) [17, 18], which is equivalent to 0.57 m of delay at L1 frequency. Higher values for all three quantities are found for large-scale TIDs [19, 20]. Using GPS data from dense networks of ground receivers, TID wave-front widths of 2000 km were measured [20, 21]. The wide range of values for TID wavelength, velocity, and amplitude highlight the unpredictability of this source of satellite ranging error.

B. Nominal Model for the Main Trend of the Ionospheric Delay

A piecewise linear model of the vertical ionospheric delay under anomaly-free conditions in mid-latitude regions was derived in [4]. The model hinges on three major assumptions.

- The ionosphere is assumed constant over short periods of times in a geocentric solar magnetospheric (GSM) frame (whose x-axis points toward the sun and whose z-axis is the projection of the earth's magnetic dipole axis on to the plane perpendicular to the x-axis) [22].
- A spherical thin shell approximation is adopted to localize the effect of the ionosphere at the altitude h_I of the expected peak in electron density ($h_I=350$ km). An ionospheric pierce point (IPP) is defined as the intersection between the satellite LOS and the thin shell.
- The vertical ionospheric delay varies linearly with IPP separation distances d_{IPP} [23], for d_{IPP} smaller than a limit $d_{IPP,MAX}$ of 750 km [4]. The distribution of the corresponding slope can be bounded by a Gaussian model [24].

Thus, the ionospheric delay at epoch k is modeled as an initial vertical ionospheric bias b_{VI} associated with a ramp, whose constant slope over $d_{IPP,k}$ is the vertical ionospheric gradient g_{VI} . An obliquity factor $c_{OI,k}$ accounts for the fact that the LOS pierces the ionosphere with a slant angle function of the satellite elevation angle θ_k (e.g., [25]). The coefficient $c_{OI,k}$ is expressed

as:

$$c_{OI,k} = \left(1 - [R_E \cos \theta_k / (R_E + h_I)]^2\right)^{-1/2}, \quad (28)$$

where R_E is the radius of the earth (h_I is defined above). As a result, the slant ionospheric delay (for code) or advance (for carrier) is given by:

$$\varepsilon_{I,k} = c_{OI,k} (b_{VI} + d_{IPP,k} g_{VI}). \quad (29)$$

Equation (29) is applied to 750 km-long segments of IPP displacements for each visible SV (see [4] for details). It assumes that IPPs follow straight paths along the great circle over short time periods. The model is applicable to both GPS and LEO SV signals because $d_{IPP,k}$ is evaluated in a GSM frame fixed to the sun, the source of the ionosphere's main variations (the motion of the earth is implicitly accounted for). Bounds on the prior probability distributions of b_{VI} and g_{VI} are given by (using the notation defined in (9)):

$$b_{VI} \sim \mathcal{N}(0, \sigma_{VIB}^2) \quad \text{and} \quad g_{VI} \sim \mathcal{N}(0, \sigma_{VIG}^2). \quad (30)$$

A linear model of the vertical ionospheric delay similar to (29) was previously used for snapshot applications in [23, 26, 27]. In this case, there was no need to make assumptions on the motion of the ionosphere, the user antenna and the satellite (and the IPP separation distance did not need to be referenced in a GSM frame). The model was evaluated using experimental data collected at WAAS ground stations and at CORS sites during ionospherically quiet and active days from 1999 to 2004. Estimates of σ_{VIG} , of σ_{VIB} and of residual mis-modeling errors were established in [3] using the results of [26, 27] and using WAAS performance analysis reports [28] from spring 2002 to spring 2008. These estimates are only valid for ionospherically quiet to active days. A storm-detector would have to be implemented to ensure the system's integrity under stormy conditions, but this is beyond the scope of this paper.

In this work, the ionospheric error model in (29) is evaluated against a set of ionospheric delay measurements collected between January and August 2007 at the CORS site in Holland, Michigan. The model proved to accurately match the data for satellite signal elevation angles

higher than 50 deg in [4]. However in Fig. 1, although the largest part of the ionospheric delay is efficiently removed, substantial mis-modeling errors remain that are caused by TIDs affecting low elevation measurements. A new model is derived in an attempt to mitigate the impact of these TIDs.

C. New Ionospheric Error Model Accounting for TIDs

The experimental evaluation in Sec. V-D establishes that a substantial percentage of GPS satellite passes are affected by TIDs. Therefore, TIDs can not be considered rare-event faults for high-integrity applications and must be part of the nominal FF model.

The new model for the ionospheric delay is the sum of the nominal model in (29), which captures the main trend of the ionosphere, and a sinusoidal wave, which accounts for TIDs. The sine-wave's amplitude is modulated by the obliquity coefficient $^s c_{OI,k}$. The proposed model is written as:

$$\begin{aligned} \varepsilon_{I,k} = c_{OI,k} & \left[b_{VI} + d_{IPP,k} g_{VI} \right] \\ & + c_{OI,k} \left[a_C \cos(\omega_I d_{IPP,k}) + a_S \sin(\omega_I d_{IPP,k}) \right], \end{aligned} \quad (31)$$

where ω_I is the TID frequency (in radians per length of IPP displacement), and a_C and a_S are the amplitudes of the TID's cosine and sine terms in the vertical direction (i.e., perpendicularly to the ionospheric thin shell). The sum of sine and cosine terms in (31) is equivalent to a single cosine term with amplitude a and phase ϕ :

$$a \cos(\omega_I d_{IPP,k} + \phi), \quad (32)$$

where $a \cos \phi = a_C$ and $-a \sin \phi = a_S$. The expression in (31) is preferred because it only includes one non-linear parameter ω_I for the vertical delay versus two in (32) with ω_I and ϕ .

The new model in (31) accounts for the main trend of the ionosphere as well as for spatially-varying quasi-periodic residual errors observed in the lower part of Fig. 1. The assumption of a dominant single wave period is based on the literature reviewed in Sec. IV-A, in which researchers seek to estimate characteristic TID frequencies and amplitudes. The model's

frequency and amplitude parameters (ω_l , a_c and a_s) are assumed constant over short time periods, but they are unknown. Their probability distributions are established in Sec. V using experimental data and can be exploited as prior knowledge in the estimation algorithm in (4).

In addition, the model in (31) uses a single frequency parameter ω_l rather than multiple Fourier basis functions. The reason for that choice stems from the following tradeoff: a more complex model may further reduce residual errors, but it would also increase the uncertainty of the ranging measurement in (1) and hence cause a reduction in the navigation system's availability. The next step in Sec. V is to assess the fidelity of the nominal and of the new model to experimental data from CORS.

V. EXPERIMENTAL IONOSPHERIC MODEL ANALYSIS

Dual-frequency GPS data are exploited in this section to analyze ranging errors caused by the ionosphere on single-frequency GPS and LEO measurements. Processing methods implemented to fit the nominal and new error models to the data are described in Sec. V-A, B and C. These methods are employed in Sec. V-D to analyze TIDs. The two ionospheric error models are then evaluated over varying lengths of the fit interval, which is limited in time in Sec. V-E, and is limited in IPP displacement in Sec. V-F (these two subsections respectively investigate the impact of ionospheric errors on GPS and LEO observations).

The set of GPS data selected in this analysis was collected over 91 days of quiet ionospheric activity (A_K -indexes ranging between 1 and 3 [10]) between January and August 2007, at seven different CORS sites spread across the United States (listed in Table I). The choice of quiet days in 2007, a year of low activity in the 11 year-long solar cycle, will provide rather optimistic results under 'ideal' ionospheric conditions. If the new model in Sec. IV-C does not robustly match the data even under these 'ideal' conditions, then the new model will be set aside and the bounding bias method of Sec. III will be adopted.

A. *Experimental Data Processing Method*

The ionospheric delay is proportional to the total electron content in the path of the signal and

to the inverse square of the carrier frequency. This frequency-dependence is exploited here with dual-frequency satellite signals to measure ionospheric disturbances. Measurement error models are then derived and implemented to account for the ionosphere's impact on single-frequency user receiver observations.

Dual-frequency GPS carrier-phase observations (noted ϕ_{L1} and ϕ_{L2} , in units of meters, at frequencies $f_{L1} = 1575$ MHz and $f_{L2} = 1228$ MHz) are processed to evaluate the ionospheric delay on L1 signals (at f_{L1} frequency). The following frequency coefficient is used in the derivation:

$$c_{L1} = f_{L2}^2 / (f_{L1}^2 - f_{L2}^2) \quad (33)$$

A biased and noisy measure of the ionospheric delay is obtained by differencing L1 and L2 observations (see [25] for example):

$$z_{I,k} = c_{L1}(\phi_{L1,k} - \phi_{L2,k}) = \varepsilon_{I,k} + b_I + v_{I,k}, \quad (34)$$

where b_I is a constant bias that includes the differenced L1-L2 cycle ambiguity and inter-frequency biases. The measurement noise $v_{I,k}$ is a time-correlated random sequence (due to differenced carrier multipath and receiver noise) such that:

$$v_{I,k} \sim N(0, \sigma_I^2),$$

where the standard deviation σ_I is conservatively estimated to be about 5 cm.

The value of 5 cm is obtained by linearly detrending sequences of differenced carrier measurements $z_{I,k}$ over 15-min-long time intervals in order to isolate the $v_{I,k}$ term. The 15 min period was assumed to be longer than the multipath correlation time constant, so that multipath error is not eliminated. But 15 min is also shorter than time periods of both the low and high-frequency ionospheric contents in $\varepsilon_{I,k}$, which is hence removed from $z_{I,k}$ in (34) (b_I is constant and is eliminated by detrending). The standard deviation σ_I depends on the CORS receiver, on the environment surrounding the CORS antenna and on satellite elevation. The value of σ_I was evaluated using eight months of data at two locations (the Holland and Miami stations, equipped

with different receivers and antennas) and varied between 5 cm for satellite elevation angles lower than 20 deg, to 1 cm at elevation angles higher than 50 deg. For clarity of explanation, and because the largest TIDs are observed at low elevation angles, the σ_I value of 5 cm is retained.

Models of the ionospheric delay are evaluated using the measurement in (34). The residual errors, after removing the estimated delay from the actual data, are the sum of the measurement error $v_{I,k}$ and the modeling error.

TABLE I
CORS SITES USED FOR MODEL EVALUATION

Site Location	Latitude (deg N)	Longitude (deg E)
Battle Creek, Michigan	43.31	-86.20
Holland, Michigan	42.79	-86.11
Cleveland, Ohio	41.48	-81.67
Miami, Florida	25.78	-80.22
Houston, Texas	29.76	-95.38
Los Angeles, California	34.05	-118.25
Salt Lake City, Utah	40.75	-111.88

B. Nominal Model Parameter Estimation

A batch least-squares measurement equation is obtained by substituting the nominal model of $\varepsilon_{I,k}$ in (29) into (34) and stacking observations $z_{I,k}$ in order to simultaneously estimate the three constant parameters b_I , b_{VI} and g_{VI} (Klobuchar model corrections [29] are first applied to $z_{I,k}$):

$$\begin{bmatrix} z_{I,0} \\ \mathbf{M} \\ z_{I,k_F} \end{bmatrix} = \begin{bmatrix} 1 & c_{OI,0} & c_{OI,0} d_{IPP,0} \\ \mathbf{M} & \mathbf{M} & \mathbf{M} \\ 1 & c_{OI,k_F} & c_{OI,k_F} d_{IPP,k_F} \end{bmatrix} \begin{bmatrix} b_I \\ b_{VI} \\ g_{VI} \end{bmatrix} + \begin{bmatrix} v_{I,0} \\ \mathbf{M} \\ v_{I,k_F} \end{bmatrix}. \quad (35)$$

Equation (35) is in the form of (2). Time-correlated noise due to multipath is modeled as a first order Gauss Markov process with time constant T_M . Consider the covariance matrix \mathbf{V} of the

measurement noise vector \mathbf{v} in (2). The raw carrier phase receiver noise and multipath (at L1 and L2 frequencies) are modeled as Gaussians with $\sigma_{RN,\phi}^2$ and $\sigma_{M,\phi}^2$, respectively (with $\sigma_{RN,\phi}^2 = 9$ mm and $\sigma_{M,\phi}^2 = 30$ mm). The time-correlation between two measurements at sample times t_i and t_j is modeled in (i, j) -elements of \mathbf{V} as $2 c_{L1}^2 \sigma_{M,\phi}^2 e^{-\Delta t_{ij}/T_M}$, where $\Delta t_{ij} = |t_i - t_j|$ and c_{L1} is the frequency coefficient defined in (33). The quantity $2 c_{L1}^2 \sigma_{RN,\phi}^2$ is also added to the diagonal elements of \mathbf{V} to account for uncorrelated carrier phase receiver noise. Prior knowledge on b_{VI} and g_{VI} is introduced assuming a-priori bounding values for their standard deviations. For the set of data under consideration, these values are defined as:

$$\sigma_{VIB,0} = 3 \text{ m} \quad \text{and} \quad \sigma_{VIG,0} = 5 \text{ mm/km}.$$

Larger values may be considered for days of higher ionospheric activity.

State estimates for b_I , b_{VI} and g_{VI} are computed using equation (4), where \mathbf{P}_{PK} is a 2×2 diagonal covariance matrix with diagonal elements $\sigma_{VIB,0}^2$ and $\sigma_{VIG,0}^2$. Unlike other procedures that assume constant obliquity $c_{OI,k}$ over short time-intervals [27], this estimation method exploits the observability provided by the relative change in coefficients $c_{OI,k}$, $c_{OI,k} d_{IPP,k}$ and 1. The prior information matrix \mathbf{P}_{PK}^{-1} is an important input that guarantees realistic b_{VI} and g_{VI} estimates in case of poor observability.

C. Parameter Estimation for the New Nonlinear Model

Substituting the new model (31) into (34) establishes a non-linear relationship between the measurement $z_{I,k}$ and a constant state vector \mathbf{x}_I to be estimated, which is noted:

$$z_{I,k} = \varepsilon_{I,k}(\mathbf{x}_I) + v_{I,k}, \quad (36)$$

where
$$\mathbf{x}_I = [b_I \quad b_{VI} \quad g_{VI} \quad a_C \quad a_S \quad \omega_I]^T. \quad (37)$$

Initial guesses of the states $b_{I,0}$, $b_{VI,0}$, $g_{VI,0}$, $a_{C,0}$, $a_{S,0}$ and $\omega_{I,0}$ (listed in Table II) are iteratively refined using the Newton Raphson method. At the j^{th} iteration, (36) can be linearized about

estimated parameter values $b_{I,j}$, $b_{VI,j}$, $g_{VI,j}$, $a_{C,j}$, $a_{S,j}$ and $\omega_{I,j}$ that are arranged in a vector $\mathbf{x}_{I,j}$ akin to (37). The vector $\delta\mathbf{x}_{I,j}$ of deviations between the true and estimated state parameters is defined as:

$$\delta\mathbf{x}_{I,j} = [\delta b_I \quad \delta b_{VI} \quad \delta g_{VI} \quad \delta a_C \quad \delta a_S \quad \delta \omega_I]_j^T. \quad (38)$$

The linearized measurement equation becomes:

$$\delta z_{I,k,j} = \nabla \varepsilon_{I,k,j}^T \delta\mathbf{x}_{I,j} + v_{I,k}, \quad (39)$$

where

$$\delta z_{I,k,j} = z_{I,k} - f_k(\mathbf{x}_{I,j}) \quad (40)$$

and

$$\nabla \varepsilon_{I,k,j} = \left[1 \quad \frac{\partial \varepsilon_{I,k}}{\partial b_{VI}} \quad \frac{\partial \varepsilon_{I,k}}{\partial g_{VI}} \quad \frac{\partial \varepsilon_{I,k}}{\partial a_C} \quad \frac{\partial \varepsilon_{I,k}}{\partial a_S} \quad \frac{\partial \varepsilon_{I,k}}{\partial \omega_I} \right]_j^T \quad (41)$$

with

$$\frac{\partial \varepsilon_{I,k}}{\partial b_{VI}} = c_{OI,k}, \quad \frac{\partial \varepsilon_{I,k}}{\partial g_{VI}} = c_{OI,k} d_{IPP,k}, \quad (42)$$

$$\frac{\partial \varepsilon_{I,k,j}}{\partial a_C} = c_{OI,k} \cos(\omega_{I,j} d_{IPP,k}), \quad (43)$$

$$\frac{\partial \varepsilon_{I,k,j}}{\partial a_S} = c_{OI,k} \sin(\omega_{I,j} d_{IPP,k}), \quad (44)$$

$$\begin{aligned} \frac{\partial \varepsilon_{I,k,j}}{\partial \omega_I} &= c_{OI,k} d_{IPP,k} a_{S,j} \cos(\omega_{I,j} d_{IPP,k}) \\ &\quad - c_{OI,k} d_{IPP,k} a_{C,j} \sin(\omega_{I,j} d_{IPP,k}) \end{aligned} \quad (45)$$

TABLE II

NOMINAL PARAMETER VALUES FOR THE NEW IONOSPHERIC ERROR MODEL

Parameter	Nominal Value	Parameter	Nominal Value
$b_{VI,0}$	2 m	$\sigma_{VI,0}$	3 m
$g_{VI,0}$	0 mm/km	$\sigma_{VI,0}$	5 mm/km
$a_{C,0}$	0 m	$\sigma_{aC,0}$	1 m
$a_{S,0}$	0 m	$\sigma_{aS,0}$	1 m
$\omega_{I,0}$	$21 \cdot 10^{-3}$ rad/km	$\sigma_{\omega I,0}$	$3 \cdot 10^{-3}$ rad/km
$b_{I,0}$	0 m		

Measurement deviations $\delta z_{I,k,j}$ are stacked in a batch:

$$\delta \mathbf{z}_{I,j} = \begin{bmatrix} \delta z_{I,0} \\ \mathbf{M} \\ \delta z_{I,k_F} \end{bmatrix}_j = \begin{bmatrix} \nabla \varepsilon_{I,0}^T \\ \mathbf{M} \\ \nabla \varepsilon_{I,k_F}^T \end{bmatrix}_j \delta \mathbf{x}_{I,j} + \begin{bmatrix} v_{I,0} \\ \mathbf{M} \\ v_{I,k_F} \end{bmatrix}_j. \quad (46)$$

The weighted pseudo-inverse matrix \mathbf{S}_j of $[\nabla \varepsilon_{I,0} \ \cdots \ \cdots]_j^T$ is again derived using (4). In this case, \mathbf{P}_{PK} is a 5×5 diagonal covariance matrix with diagonal elements $\sigma_{VIB,0}^2$, $\sigma_{VIG,0}^2$, $\sigma_{aC,0}^2$, $\sigma_{aS,0}^2$, and $\sigma_{aI,0}^2$ (values also listed in Table II). The covariance matrix \mathbf{V} of the measurement vector is identical to Sec. V-B.

It is worth noticing that the values listed in Table II were selected for the set of data analyzed in this work (during the solar minimum). The initial iterate values and their standard deviations would be subject to change for different periods of the solar cycle, not to mention time of day, latitude, longitude and other TID-influencing parameters. However, a more distant initial guess is expected to only increase the number of iterations while continuing to converge to the same solution.

The state estimate vector $\mathbf{x}_{I,j}$ is updated following the equation:

$$\mathbf{x}_{I,j} = \mathbf{x}_{I,j-1} + \delta \mathbf{x}_{I,j} \quad (47)$$

where

$$\delta \mathbf{x}_{I,j} = \mathbf{S}_j \delta \mathbf{z}_{I,j}.$$

Batch measurement updates are repeated until the convergence criterion is met:

$$|J_{j+1} - J_j| < \xi \quad (48)$$

where

$$J_j = \delta \mathbf{z}_{I,j}^T \mathbf{V}^{-1} \delta \mathbf{z}_{I,j}. \quad (49)$$

A value of 0.007 was allocated to ξ , so that convergence is achieved for most satellite passes while maintaining low residual errors. If the convergence criterion in (48) is not met within a limited number of iterations, the estimation process is stopped, and the model for this sequence of measurements is categorized as non-converging. In this implementation, the number of iterations is limited to 300 to reduce the computational load while still enabling the large majority of processed measurement sequences to converge. In practice, using the set of data described in this section's introduction, the typical number of iterations to achieve convergence is lower than 50. Non-converging cases are illustrated and analyzed below for an example residual error profile.

D. Experimental TID Analysis

The first step in this experimental investigation is to confirm that the ionosphere is the cause of wave-like structures affecting sequences of observations $z_{I,k}$ in (34) (one example is identified in Fig. 1). Time-correlated measurement error due to multipath is excluded as the source of disturbance because waves do not consistently appear on daily-repeated SV trajectories. In addition, their amplitudes and wavelengths exceed 10 cm and 10 min respectively, which are too high to be attributed to multipath error [25]. Waves are simultaneously observed at nearby sites (e.g., Battle Creek and Holland, Michigan) equipped with different antennas and receivers, which excludes ground equipment malfunctions. They are also found to affect signals from different satellites crossing same sections of the sky. All these clues strongly suggest that the ionosphere is the source of wave-like structures.

Individual profiles of residual errors can be analyzed. The wave-like structure observed in Fig. 1 exhibits an approximate wavelength of 350 km (computed in a GSM frame), and an amplitude of about 20 cm, which is consistent with medium-scale TIDs [14]. It is worth noting that in most GPS-based studies, elevation cutoff angles are set higher than 30deg (30deg in [14], 40 deg in [17], 45 deg in [21], 50 deg in [5], 60 deg in [18, 20]). In contrast, in our data analysis, a 10 deg elevation mask is implemented. This may explain why large TID amplitudes (exceeding 0.4 m) are observed, even during quiet days.

Finally, a large scale analysis is performed to determine the likelihood that a GPS satellite pass is affected by a TID. The eight-month long set of data collected for all visible SVs at the seven CORS stations listed in Table I are detrended over 750 km-long IPP displacements using the nominal model (same procedure as in Fig. 1). A segment of a SV pass containing a TID is identified when one or more sample residual error exceeds a 10 cm threshold. For this set of data, 567 out of the total 57,478 segments contained a wave-like structure, which means that 0.99% of all 750 km long segments were affected by TIDs.

E. Evaluation Over a Finite Time Interval

A 10 min limit on smoothing duration T_F was fixed in [3] and [4] to ensure validity of measurement error models (including the satellite clock and orbit ephemeris errors). Over 10 min, GPS satellite IPPs travel less than the $d_{IPP,MAX}$ value of 750 km [4]. Therefore, in this subsection, satellite passes are divided into segments of 10 min duration.

Residual errors are computed using both the nominal model and the new model. The complete eight-month-long set of data (for all SVs and locations listed in Table I) is detrended over 201,039 segments of 10 min length, with a 30 s sample interval (which represents a total of 4,221,819 samples). The folded cumulative distribution functions (CDFs) of residual errors using both models are plotted in Fig. 2 (thick lines), together with over-bounding Gaussian functions (thin lines). Folded CDFs represent a standard CDF for cumulative probabilities lower than 0.5 and 1-CDF for larger cumulative probabilities.

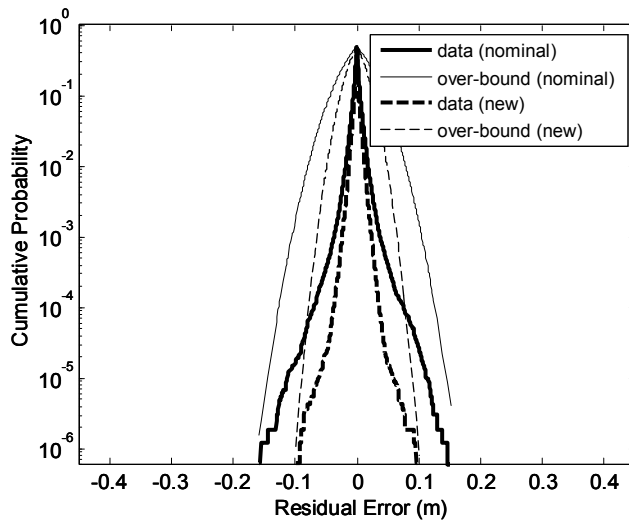


Fig. 2. Folded CDF of Ionospheric Delays Detrended Over 10min

Fig. 2 shows the improvement achieved using the new model (dashed lines) as compared to the nominal model (solid lines). The CDF for the new model is much tighter. Maximum residual values are reduced from 23.2 cm to 13.2 cm. The standard deviations of the over-bounding

functions are 4.7 cm and 2.65 cm for the nominal and new models, respectively. These values (dominated by residual errors from low elevation satellite signals) are lower than the 5 cm measurement noise standard deviation (σ_l). It suggests that mis-modeling errors are small relative to measurement noise (i.e., in this case, mis-modeling errors are at the centimeter level).

F. Evaluation Over Limited IPP Displacements

Ionospheric error models derived in Sec. IV apply to both GPS and LEO satellites because they are expressed as a function of IPP displacements d_{IPP} in a GSM frame. Complete LEO satellite passes can reach d_{IPP} -lengths of 3300 km within 10 min. In reference [4], LEO satellite passes were divided into $d_{IPP,MAX}$ -long segments (with $d_{IPP,MAX}=750$ km) so that the vertical ionospheric delay linearity assumption remained valid.

In this subsection, dual-frequency data from GPS satellites are used to evaluate ionospheric errors affecting LEO satellite signals over 750 km-long segments (actual LEO data will be processed in future work). GPS satellites take 20 min to 40 min to reach IPP displacements of 750 km. Residual errors are again computed using the two ionospheric delay models. The complete data set is detrended over 57,478 segments of 750 km length (which represents a total of 3,777,406 samples).

Folded CDFs (thick lines) and bounding Gaussian functions (thin lines) of the residual errors are given in Fig. 3 for the new (dashed) and nominal (solid) models. The folded CDFs are expectedly wider in Fig. 3 than in Fig. 2 because of the two to four-times longer fit interval. The new model provides substantial improvement. The standard deviation of the over-bounding Gaussian function decreases from 8.2 cm with the nominal model to 5.7 cm.

The maximum residual for the new model was 27.2 cm versus 39.8 cm for the nominal model. The segment containing this last 40 cm residual error is plotted in Fig. 4 and shows how effective the new model (dashed line) can be. For this particular detrended delay profile (recorded for PRN 20 on 01/08/2007 starting at 10:14 am local time in Cleveland, Ohio), the maximum residual error was decreased by a factor of four.

However, there are a few cases (168 cases representing 0.29% of all segments) where the Newton-Raphson convergence criterion in (48) could not be fulfilled within the predefined maximum number of iterations. The residual error profile for one of these non-converging cases (PRN 10 on 01/22/2007 at 11:11 am local time in Salt Lake City, Utah) is displayed in Fig. 5, where the data was detrended using the nominal model. The observed structure is not sinusoidal and its peak-to-valley variation exceeds 35 cm. This is evidence of the unpredictability of ionospheric disturbances, even in mid-latitude regions, during quiet days and at a low point in the solar cycle activity (i.e., under ideal ionospheric conditions).

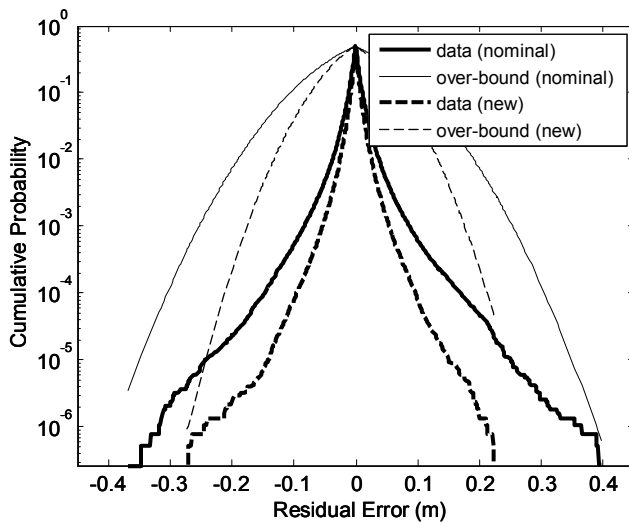


Fig. 3. Folded CDF of Ionospheric Delays Detrended Over 750 km

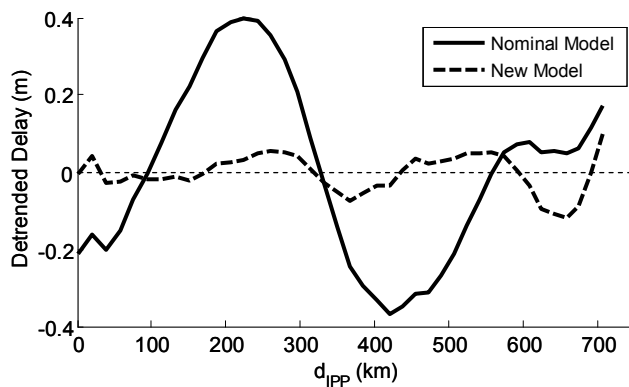


Fig. 4. Example Residual Error Profile for the Nominal and New Models Over 750 km

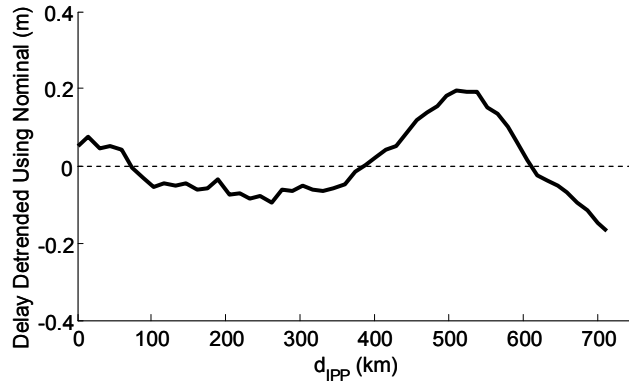


Fig. 5. Residual Error Profile of a Non-Converging Case Over for a 750 Km-Long Fit Interval

In addition, despite the improvement brought by the new model in Fig. 3, the standard deviation of the over-bounding Gaussian function of 5.7 cm (thin dashed line) is larger than the conservative measurement noise standard deviation of 5 cm. In this case, mis-modeling errors are not negligible with respect to measurement noise, which means that the new model does not robustly account for ionospheric errors, even under ideal conditions.

In summary for Sec. IV and V, experimental data analysis has demonstrated that ionospheric delay variations are extremely challenging to capture through simple modeling. This is particularly relevant when considering ionospheric errors affecting fast-moving LEO satellite signals (as shown in Sec. V-F). The new model brings about significant improvement, but substantial mis-modeling errors remain.

Therefore, in the rest of the paper, we implement the nominal bias-and-gradient model, which has been validated in [3] using large sets of data processed in [26-28] (not limited to days of quiet ionospheric activity, as explained in Sec. IV-B). Residual errors after removing the nominal model from the data have been shown to reach up to 40 cm in Fig. 3 and 4 (thick solid lines) and medium-scale TID amplitudes of up to 60 cm have been observed in [17, 18]. The impact of potential TID-induced residual errors on overall system performance is evaluated in Sec. VI.

VI. MULTI-CONSTELLATION AVAILABILITY PERFORMANCE ANALYSIS

A. TID Mitigation Techniques for Single-Frequency Implementations

Accounting for TIDs plays a crucial part in the availability performance evaluation. TIDs are frequently-occurring, temporary, localized and moving wave-like structures that are highly unpredictable. TID modeling approaches were investigated in Sec. IV and V. In order to reduce the mis-modeling errors quantified in Fig. 3, more robust ionospheric error models could be implemented. However, this method is limited because each new parameter added to the model introduces uncertainty in the estimation algorithm, which ultimately causes loss of availability.

As an alternative, ground correction and monitoring of the ionosphere against TIDs was also considered. Fig. 6 displays IPP locations (computed in a GSM frame) over a 10 min period for a network of 28 ground receivers co-located with WAAS reference stations. GPS IPP separation distances are too large to robustly detect structures at the 100-300 km scale (typical TID wavelength). The snapshot of IPP coverage in Fig. 6 demonstrates that even if Iridium signals were used, large sections of the sky remain uncovered.

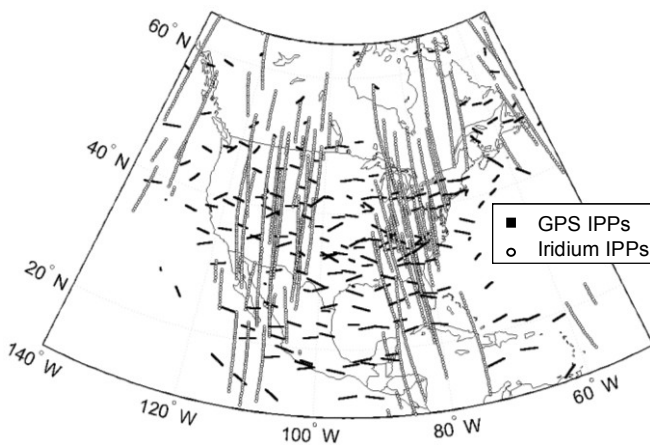


Fig. 6. IPP Coverage of a WAAS-Like Network of Ground Stations Over 10min Using GPS and Assumed Iridium Measurements

B. Sensitivity to TID Mis-Modeling Errors

Instead, in this paper, residual errors caused by TIDs are conservatively accounted for using an upper bound method derived in Sec. III. Vertical protection levels (VPLs) at touchdown are plotted in Fig. 7 for aircraft approaches simulated over a 24 hour period, for a 10 min smoothing interval T_F , for the Iridium/GPS constellation at the Miami location, which is a near-worst location as explained in Appendix II. The wide-area differential, single-frequency Iridium/GPS navigation system description, the VPL derivation and the parameters used in the performance evaluation are detailed in Appendices I and II. The VPL saw-tooth pattern in Fig. 7 is explained as follows: low VPLs are achieved at the seam of the Iridium constellation where the orbital plane separation angle is smaller (corresponding to about 9-10 hr and 21-22 hr on the x-axis); the Miami location crosses an Iridium orbital plane every two hours, which generates regularly-spaced valleys in VPL (see [3] for further details). These observations demonstrate that Iridium satellite signals are the driving force in Iridium/GPS performance.

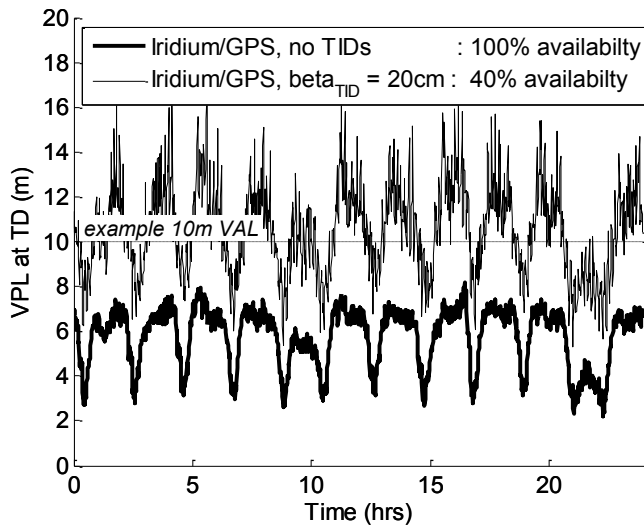


Fig. 7. Impact of TIDs on FF-Availability for an Iridium/GPS System

Fig. 7 shows that, assuming no occurrence of TIDs (thick line), VPLs remain lower than the example VAL requirement of 10 m, so that FF-availability is 100%. In parallel, VPLs are estimated assuming that single-satellite TIDs could alter ranging signals at all times during each approach. A β_{TID} -parameter value of 20 cm is implemented in (20) to compute an upper-bound b on the mis-modeling error, which causes a dramatic drop in availability from 100% to 40% for the example 10 m VAL. Fig. 7 suggests that TIDs will heavily impact the FF performance.

In addition, experimental data in Sec. V-F showed that, even during days of quiet ionospheric activity, higher β_{TID} -values could be expected (residual errors of up to 40 cm were observed). Also, about 1% of satellite passes processed in Sec. V-D was affected by TIDs with amplitudes larger than 10 cm: the likelihood of a TID affecting multiple SVs is not negligible, especially in the context of multi-constellation navigation systems.

Therefore, to further investigate the availability performance sensitivity to mis-modeling errors, the impact of TIDs simultaneously affecting multiple satellites is analyzed in Fig. 8-a, 8-b and 8-c for example VAL requirements of 10 m, 20 m and 30 m, respectively. The range of TID amplitudes under consideration reaches up to 60 cm, which is the largest value found in the literature for medium-scale TIDs [17, 18]. Also, we consider that TIDs may appear at anytime, so that their assumed probability of occurrence is 100% (for each case where the TID affects one, two or all SV signals).

Fig. 8-c shows that, in the case of TIDs impacting a single satellite signal at a time (solid line), FF-availability of 98% can be achieved for a 30 m VAL, for TID amplitudes of up to 60 cm. However, assuming that TIDs could simultaneously affect two SVs (dashed line), availability drops below 98% for TID amplitudes larger than 35 cm. And it drops below 90% for TID amplitudes of as small as 12 cm in the worst theoretical case where satellite signals are all simultaneously impacted by TIDs (which is unlikely to occur).

A more stringent 20 m VAL requirement is considered in Fig. 8-b. In the case of single SV TIDs, FF-availability is 98% for a TID amplitude of about 33 cm, as compared to 60 cm for the 30 m VAL in Fig. 8-c. This comparison demonstrates that the tighter the VAL requirement is,

the more sensitive the availability performance to TID mis-modeling errors will be.

Finally, Fig. 8-a displays extremely poor availability results for the example 10 m VAL requirement, even for TID amplitudes smaller than 15 cm and assuming TIDs affecting one SV at a time. In this case, combined FF-SSF availability, computed using (21), (23) and (27), is even lower. The result in Fig. 8-a is strong evidence that non-differential, single-frequency Iridium/GPS is not sufficient in applications that require VALs of 10 m or lower. For this reason, in the next subsection the performance of future dual-frequency implementations is assessed.

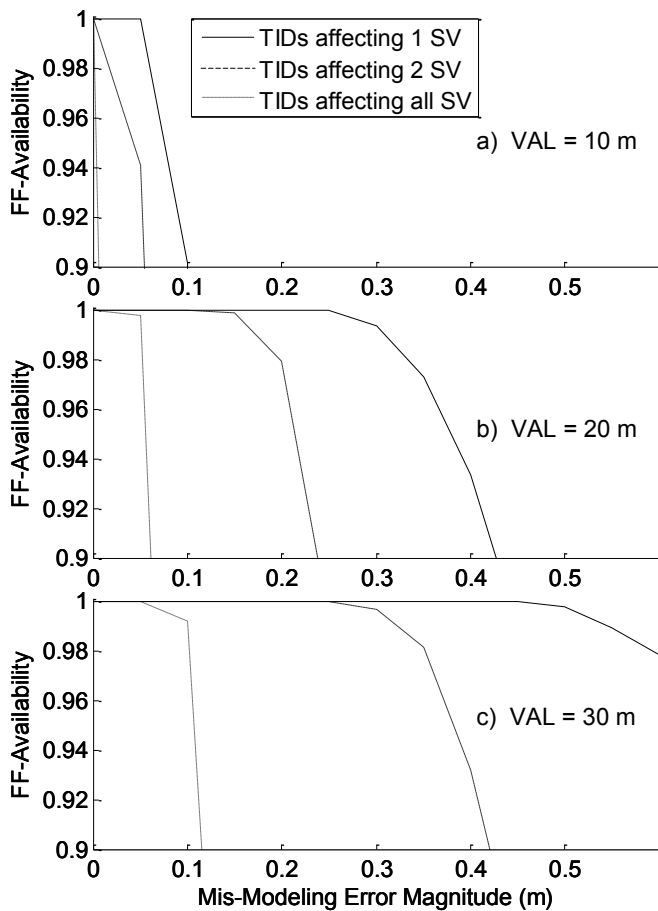


Fig. 8. Availability Sensitivity to TID Amplitude at the Miami Location for (a) VAL = 10m, (b) VAL = 20m and (c) VAL = 30m

C. Future Dual-Frequency Multi-Constellation Navigation Systems

Dual-frequency implementations may become available in the near term future as explained in Appendix II. In this subsection, dual-frequency navigation systems are considered to investigate the combined FF-SSF availability performance for a demanding 10 m VAL requirement (the combined availability criterion is defined in Appendix II). Dual-frequency measurements are free of ionospheric errors (at the cost of a slight increase in measurement noise as indicated in Appendix I). The overall performance of future dual-frequency multi-constellation navigation systems is evaluated in Fig. 9 against step and ramp-type faults of all magnitudes and start times. Combined FF and SSF availability is presented for a 5 deg \times 5 deg latitude-longitude grid of locations over the contiguous United States (CONUS), for a 10 m VAL and for a smoothing period T_F that was decreased to 5 min (the shorter the smoothing period is, the more practical and computationally-efficient the implementation will be).

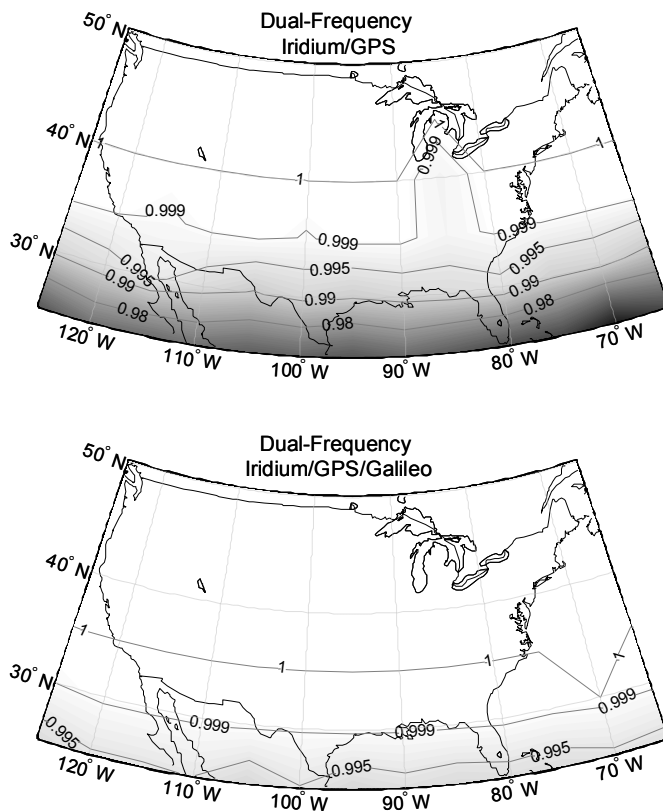


Fig. 9. Sensitivity of Combined-Availability to Constellation and Location, for a 10 m VAL and a 5 min Smoothing Period

Results for the GPS/Galileo system were very poor and are not represented. This highlights again that large Iridium satellite motion is instrumental in meeting a 10 m VAL requirement. Combined availability for the two Iridium-augmented systems illustrated in Fig. 9 improves at higher latitudes, where the SV density of the Iridium near-polar constellation increases. Availability ranges between 98.4% and 100% for the Iridium/GPS system, and between 99.9% and 100% for Iridium/GPS/Galileo. Both Iridium-augmented GNSS produce maximum availability if the smoothing period T_F is increased to 10 min. This result illustrates the potential of Iridium-augmented GNSS to fulfill demanding navigation requirements specified in high-integrity aviation applications.

These results were computed under the assumption that the satellite clock and orbit and tropospheric error models were robust over short time periods. Also, ramps and steps do not constitute a comprehensive description of all potential integrity threats. Future work includes further refinement of measurement error and fault models.

VII. CONCLUSION

The combination of redundant ranging signals from multiple satellite constellations opens the possibility for high-integrity positioning over wide areas. Multi-constellation navigation systems provide geometric diversity, which can be exploited by filtering carrier phase measurements over time.

In this paper, ionospheric error models for both GPS and LEO satellite signals were experimentally evaluated using dual-frequency GPS data collected at multiple CORS sites over an eight-month long period. A new model was derived to account for frequently-occurring, localized, temporary wave-like structures that were demonstrated to be travelling ionospheric disturbances (TIDs). The improvement brought by the new model over a previously-validated nominal model was quantified. However, when considering ionospheric delays affecting fast-moving LEO satellite signals, significant mis-modeling errors were obtained even during days of

quiet ionospheric activity.

In response, a conservative approach to account for the unknown time-behavior of residual mis-modeling errors was devised. It was implemented in conjunction with the nominal ionospheric error model to demonstrate that the navigation system performance would be heavily impacted by TIDs. In particular, availability performance evaluations provided evidence that wide-area-differential, single-frequency Iridium/GPS would not be sufficient to achieve a stringent 10 m vertical alert limit (VAL), but could be employed in applications that require a 30 m VAL under non-stormy ionospheric conditions.

Dual-frequency implementations that might become available in the near-term future were also investigated. Overall system performance sensitivity was quantified over CONUS, for three multi-constellation navigation systems (GPS/Galileo, Iridium/GPS and Iridium/GPS/Galileo). It showed that the two dual-frequency Iridium-augmented GNSS could potentially achieve 100% availability at all CONUS locations, even for a tight 10 m VAL.

APPENDIX I. MEASUREMENT ERROR MODEL PARAMETERS

The error model state vector \mathbf{x}_{ERR} in (3), assuming the nominal ionospheric model in (29), is expressed as:

$$\mathbf{x}_{ERR} = [\mathbf{b}_{VI}^T \quad \mathbf{g}_{VI}^T \quad \mathbf{b}_{SVOC}^T \quad \mathbf{g}_{SVOC}^T \quad b_{ZT} \quad \Delta n]^T,$$

where individual error state vectors \mathbf{b}_{VI} , \mathbf{g}_{VI} , \mathbf{b}_{SVOC} , and \mathbf{g}_{SVOC} include the error states for all n_s visible satellites (for example, for \mathbf{b}_{VI} , we use the notation $\mathbf{b}_{VI} = [b_{VI}^1 \quad \dots \quad b_{VI}^{n_s}]^T$). The prior knowledge matrix \mathbf{P}_{PK}^{-1} on \mathbf{x}_{ERR} is diagonal, with diagonal vector:

$$[\mathbf{1}_{1 \times n_s} \sigma_{VIB}^{-2} \quad \mathbf{1}_{1 \times n_s} \sigma_{VIG}^{-2} \quad \mathbf{1}_{1 \times n_s} \sigma_{SVOC,B}^{-2} \quad \mathbf{1}_{1 \times n_s} \sigma_{SVOC,G}^{-2} \quad \sigma_{ZTD}^{-2} \quad \sigma_{\Delta n}^{-2}]$$

where $\mathbf{1}_{1 \times n}$ is a $1 \times n$ row-vector of ones.

Parameters that are elements of the error state vector \mathbf{x}_{ERR} are summarized in the left hand side of Table III. These parameters are assumed to be constant over a short smoothing period

T_F . Prior knowledge on these parameters is included as bounds on their probability distributions captured by zero-mean Gaussian functions whose assumed standard deviations (after corrections from a WAAS-like network of reference stations) are also listed in Table III and justified in [4]. This prior knowledge is incorporated in the estimation algorithm through the prior information matrix \mathbf{P}_{PK}^{-1} in (4).

The assertion that error models are conservative requires that the Gaussian models over-bound the CDFs of each error sources' nominal ranging errors [30]. Alternatively, parameter values in Table III may be considered as requirements that ground corrections and user equipment should meet in order to achieve the desired system performance.

TABLE III
SUMMARY OF ERROR PARAMETER VALUES

Error State	Standard Deviation	Assumed std Value	Other Parameters	Nominal Value
b_{VI}	σ_{VIB}^*	1.5 m	$d_{IPP,MAX}$	750 km
g_{VI}	σ_{VIG}^*	4 mm/km	$\sigma_{RN,\rho}^{**}$	0.3 m
${}^s b_{SVOIC}$	$\sigma_{SVOIC,B,GPS}$ $\sigma_{SVOIC,B,IRI}$	2 m 0.1 m	$\sigma_{RN,\phi}^{**}$	0.01 m
${}^s g_{SVOIC}$	$\sigma_{SVOIC,G,GPS}$ $\sigma_{SVOIC,G,IRI}$	$6.487 \cdot 10^{-4}$ m/s $6.372 \cdot 10^{-4}$ m/s	$\sigma_{M,\rho}^{**}$	1 m
σ_{ZTD}	$\sigma_{ECB,GPS}$	0.12 m	$\sigma_{M,\phi}^{**}$	0.02 m
$\sigma_{\Delta t}$	$\sigma_{ECG,GPS}$	30	$T_{M,GPS}$	1 min
			$T_{M,IRI}$	2 s
* for dual-frequency: VIG and VIB terms are eliminated				
** for dual-frequency (at f_1 and f_2), these terms are multiplied by $\{[f_1^2/(f_1^2 - f_2^2)]^2 + [f_2^2/(f_1^2 - f_2^2)]^2\}^{1/2}$				

APPENDIX II. FRAMEWORK FOR THE PERFORMANCE ANALYSIS

The notional space, ground and user segments considered in this work is described in [3] and [4]. In addition, we assume a Galileo constellation including 27 satellites arranged in 3 regularly separated orbital planes of 9 spacecraft each, with a 56 deg inclination angle. A network of

ground stations is assumed co-located with WAAS reference stations, whose correction accuracy has been documented over the past seven years [28]. Finally, in the perspective of GPS modernization and with the emergence of new GNSS, future dual-frequency GPS and Galileo measurements are also considered. Potential dual-frequency Iridium signals are simulated as well.

A benchmark mission of aircraft precision approach is used for performance evaluations in Sec. VI. During an approach, the airplane is assumed to follow a straight-in trajectory at a constant speed of 70m/s with a 3 deg glide-slope angle towards the runway until touchdown (TD) where requirements apply. Miami is selected as a nominal location. Because of Iridium's near-polar orbits, Iridium satellite density decreases near the equator. Miami is therefore a near-worst location for CONUS. A nominal smoothing period T_F of 10 min is chosen to investigate performance variations.

Three fundamental navigation performance metrics, originating from safety-critical aviation applications, are emphasized in the integrity analysis. First, an integrity risk requirement P_{HMI} or probability of hazardous misleading information (HMI) is given a value of $2 \cdot 10^{-7}$ [31]. Second, a value of $8 \cdot 10^{-6}$ is considered for the continuity risk requirement P_C [31]. Third, availability is computed as the fraction of time that integrity and continuity requirements are fulfilled. Integrity and continuity are instantaneous measures of mission safety, whereas availability is evaluated over multiple operations.

The most harmful threats to navigation system integrity and continuity are rare-event measurement faults such as ground or user equipment malfunctions, unusual atmospheric conditions or satellite failures. In this early stage of the system design, the integrity analysis focuses on satellite faults. Reference [32] specifies that the GPS satellite failure rate Λ is 10^{-4} /hr. The prior probability P_p of an individual satellite fault occurring during the exposure period T_F is $P_p = \Lambda T_F$.

The overall integrity requirement P_{HMI} can be allocated between mutually exclusive

hypotheses of fault-free (FF) operation, single-satellite fault (SSF) conditions, and all other conditions. In this work, an integrity risk P_{MF} is set aside for cases of multiple SV faults occurring during the same time interval T_F . Multiple simultaneous faults are assumed independent events and hence have a low probability of occurrence. Therefore, the value of P_{MF} can be selected larger than the probability of two or more faults occurring during T_F , so that:

$$P_{MF} \geq 1 - \sum_{i=0}^1 C_i^{n_s} P_p^i (1 - P_p)^{n_s - i},$$

where n_s is the number of visible SVs and $C_k^{n_s}$ is the binomial coefficient. For a 10 min exposure period T_F and using measurements from ten different SVs, the probability P_{MF} is on the order of 10^{-8} . Then, an integrity budget of $\gamma(P_{HMI} - P_{MF})$ is allocated to normal FF conditions, and the remaining fraction $(1 - \gamma)(P_{HMI} - P_{MF})$ is attributed to SSF. The coefficient γ ranges between 0 and 1; a value of 0.01 is selected to improve the combined FF-SSF performance defined below.

Availability performance criteria are established for the FF and SSF hypotheses. In this work, the focus is on the vertical coordinate both because of the tighter requirements in this direction and because of the generally worse vertical positioning performance as compared to horizontal coordinates. Under normal FF conditions, the vertical protection level VPL is expressed as:

$$VPL = \kappa_{FF} \sigma_U + b,$$

where σ_U is defined in (6), and the probability multiplier κ_{FF} is the value for which the normal CDF equals $1 - \gamma(P_{HMI} - P_{MF})/2$. In Sec. VI, the TID mis-modeling error parameter b will either be set to zero (assuming no occurrence of TIDs), or it will conservatively be defined by (20). A satellite geometry is deemed available under FF conditions if and only if:

$$VPL < VAL. \quad (50)$$

In addition, SSF availability is granted if and only if:

$$P_{MD} < (1 - \gamma)(P_{HMI} - P_{MF})/P_p, \quad (51)$$

where the probability of missed detection P_{MD} is defined in (11). Equations (50) and (51) are the expressions of FF and SSF binary criteria that either validate or nullify availability for an approach.

The duration T_{AV} over which availability simulations should be carried out is an approximation of the multi-constellation repeatability period. For GPS alone, T_{AV} is one sidereal day. For Iridium/GPS, T_{AV} can be approximated to 3 solar days (see [3] for details). A method similar to the one employed in [3] is used to establish that ten sidereal days is a good approximation of T_{AV} for the Iridium/GPS/Galileo constellation. Ultimately, the percentage of approaches (starting at regular 60 s intervals) that satisfy both (50) and (51) is the measure of ‘combined FF-SSF availability’ used in the integrity analysis of Sec. VI-C.

REFERENCES

- [1] P. Hwang, “Kinematic GPS for differential positioning: resolving integer ambiguities on the fly,” NAVIGATION: J. of ION, vol. 38.1, pp.1-15, 1991.
- [2] M. Rabinowitz, B. Parkinson, C. Cohen, M. O’Connor, and D. Lawrence, “A system using LEO telecommunication satellites for rapid acquisition of integer cycle ambiguities,” Proc. IEEE PLANS, Palm Springs, CA, pp.137-145, 1998.
- [3] M. Joerger, L. Gratton, B. Pervan, and C. Cohen. “Analysis of Iridium-Augmented GPS for Floating Carrier Phase Positioning,” NAVIGATION: J. of ION, vol. 57.2, pp.137-160, 2010.
- [4] M. Joerger, J. Neale, and B. Pervan, “Iridium/GPS carrier phase positioning and fault detection over wide areas,” Proc. ION GNSS Conf., Savannah, GA, 2009.
- [5] M. Hernandez-Pajares, J. M. Juan, and J. Sanz, “Medium-scale traveling ionospheric disturbances affecting GPS measurements: Spatial and temporal analysis,” J. Geophys. Res., vol. 111, 2006.
- [6] R. Brown, “A baseline RAIM scheme and a note on the equivalence of three RAIM methods,” NAVIGATION: J. of ION, vol. 39.4, pp.127-137, 1992.
- [7] T. Walter, and P. Enge, “Weighted RAIM for precision approach,” Proc. of ION GPS Conf., Palm Springs, CA, 1995.
- [8] M. Sturza, “Navigation system integrity monitoring using redundant measurements,” NAVIGATION: J. of ION, vol. 35.4, pp.69-87, 1988.
- [9] L. P. Kuptsov, Hölder Inequality, SpringerLink Encyclopaedia of Mathematics. Berlin: Springer-Verlag, 2001.
- [10] T. Tascione, Introduction to the Space Environment. 2nd Ed. Malabar, FL: Krieger Publishing Company, 1994.
- [11] R. D. Hunsucker, “Atmospheric gravity waves generated in the high-latitude ionosphere: a review,” Rev. Geophys. and Space Phys., vol. 20.2, pp.293-315, 1982.
- [12] K. Hocke, and K. Schlegel, “A review of atmospheric gravity waves and travelling ionospheric disturbances: 1982 – 1995,” Ann. Geophys., vol. 14, pp.917–940, 1996.
- [13] G. Crowley, and I. W. McCrea, “A synoptic study of TIDs observed in the UK during the first WAGS campaign, October 10-18, 1985,” Radio Science, vol. 23, pp.905-917, 1988.

- [14] Tsugawa, T., Y. Otsuka, A. J. Coster, and A. Saito (2007), Medium-scale traveling ionospheric disturbances detected with dense and wide TEC maps over North America, *Geophys. Res. Lett.*, 34, L22101, doi:10.1029/2007GL031663.
- [15] M. J. Nicolls, M. C. Kelley, A. J. Coster, S. A. Gonzalez, and J. J. Makela, "Imaging the structure of a large-scale TID using ISR and TEC data," *Geophys. Res. Lett.*, vol. 31, 2004.
- [16] J. K. Lee, F. Kamalabadi, and J. J. Makela "Three-dimensional tomography of ionospheric variability using a dense GPS receiver array," *Radio Science*, vol. 43, 2008.
- [17] N. Kotake, Y. Otsuka, T. Tsugawa, T. Ogawa, and A. Saito, "Climatological study of GPS total electron content variations caused by medium-scale traveling ionospheric disturbances," *J. Geophys. Res.*, vol. 111, 2006.
- [18] C. C. Lee, Y. A. Liou, Y. Otsuka, F. D. Chu, T. K. Yeh, K. Hoshinoo, and K. Matunaga, "Nighttime medium-scale traveling ionospheric disturbances detected by network GPS receivers in Taiwan," *J. Geophys. Res.*, vol. 113, 2008.
- [19] F. Ding, W. Wan, L. Liu, E. L. Afraimovich, S. V. Voeykov, and N. P. Perevalova, "A statistical study of large-scale traveling ionospheric disturbances observed by GPS TEC during major magnetic storms over the years 2003 – 2005," *J. Geophys. Res.*, vol. 113, 2008.
- [20] T. Tsugawa, A. Saito, Y. Otsuka, and M. Yamamoto, "Damping of large-scale traveling ionospheric disturbances detected with GPS networks during the geomagnetic storm," *J. Geophys. Res.*, vol. 108, 2003.
- [21] E. L. Afraimovich, I. K. Edemskiy, S. V. Voeykov, Yu. V. Yasyukevich, and I. V. Zhivetiev, "The first GPS-TEC imaging of the space structure of MS wave packets excited by the solar terminator," *Ann. Geophys.*, vol. 27, pp.1521–1525, 2009.
- [22] C. Cohen, B. Pervan, and B. Parkinson, "Estimation of absolute ionospheric delay exclusively through single-frequency GPS measurements," *Proc. ION GPS Conf.*, Albuquerque, NM, 1992.
- [23] A. Hansen, J. Blanch, T. Walter, and P. Enge, "Ionospheric correlation analysis for WAAS: quiet and stormy," *Proc. ION GPS Conf.*, Salt Lake City, UT, 2000.
- [24] J. Blanch, "Using kriging to bound satellite ranging errors due to the ionosphere," PhD Dissertation, Stanford, CA: Stanford University, 2003.
- [25] P. Misra, and P. Enge, *Global Positioning System: Signals, Measurements, and Performance*, Second Edition. Lincoln, MA: Ganga-Jamuna Press, 2006.
- [26] Hansen, A., Peterson, E., Walter, T., Enge, P., "Correlation Structure of Ionospheric Estimation and Correction for WAAS," *Proceedings of the Institute of Navigation NTM*, Anaheim, CA, 2000.
- [27] J. Lee, S. Pullen, S. Datta-Barua, and P. Enge, "Assessment of nominal ionosphere spatial decorrelation for GPS-based aircraft landing systems." *J. of Aircraft*, vol.44.5, pp. 1662-1669, 2007.
- [28] NSTB/WAAS T&E Team, William J. Hughes Technical Center, "Wide-Area Augmentation System Performance Analysis Report," Atlantic City, NJ: Reports No. 5-23, 2003-2008, available online at <http://www.nstb.tc.faa.gov/DisplayArchive.htm>.
- [29] J. Klobuchar, "Ionospheric time-delay algorithm for single-frequency GPS users," *IEEE Trans. Aerospace Electronic Sys.*, vol. 23.3, pp.325-331, 1987.
- [30] B. DeCleene, "Defining pseudorange integrity – overbounding," *Proc. ION GPS Conf.*, Salt Lake City, UT, pp.1916-1924, 2000.
- [31] RTCA Special Committee 159, "Minimum Aviation System Performance Standards for the Local Area Augmentation System (LAAS)," Document No. RTCA/DO-245, Washington, DC, 2004.
- [32] Federal Aviation Administration, "Category I Local Area Augmentation System Ground Facility," FAA-E-2937A, 2002.



Mathieu Joerger (M'10) received a Master in mechatronics from the National Institute of Applied Sciences in Strasbourg, France, in 2002. He pursued studies in mechanical and aerospace engineering at the Illinois Institute of Technology (IIT) in Chicago, where he earned a M.S. degree in 2002, and a Ph.D. in 2009.

During his graduate curriculum, his topics of research included autonomous ground vehicle navigation and control, integration of carrier phase GPS with laser-scanner observations, and augmentation of GPS with LEO Iridium satellites. He has been leading the IIT research effort on iGPS since 2006. He is currently working as a Senior Research Associate at IIT on sequential RAIM algorithms, on robust laser-based positioning procedures, and on multi-constellation navigation satellite systems for high-integrity precision applications.

Dr. Joerger is a member of the ION, AIAA, and ASME. He is the 2009 recipient of the ION Bradford Parkinson award, which honors outstanding graduate students in the field of GNSS.

Jason Neale received his B.S. in aerospace engineering (2007), and M.S. in mechanical and aerospace engineering in 2010 both from the Illinois Institute of Technology, Chicago, Illinois.

He was a Research Assistant at the Illinois Institute of Technology from 2007 to 2010, focusing on ionospheric error modeling for high integrity carrier phase positioning. He is now a Systems Engineer for L3 Communications in Hollywood, Maryland working on GPS-based precision landing systems.

Jason is a member of the ION and of the AIAA.



Seebany Datta-Barua (M'10) received her B.S. in physics (2000), and M.S. (2002) and Ph.D. (2008) degrees in aeronautics and astronautics, all from Stanford University, Stanford, California.

She was a Research Engineer at Atmospheric and Space Technology Research Associates (ASTRA) from 2008 to 2009. She is now an Assistant Professor of Aviation and Technology in the College of Engineering at San Jose State University in San Jose, California. Her research interests are in space weather forecasting through imaging and dynamics estimation of the ionosphere and in mitigating atmospheric effects on navigation systems.

Dr. Datta-Barua is a member of AGU, ION, and AIAA. She was the recipient of the ION Student Paper Award (2004) and the Stanford President's Scholar Award (1996).



Boris Pervan received a B.S. from the University of Notre Dame in 1986, M.S. from the California Institute of Technology in 1987, and Ph.D. from Stanford University in 1996, all in aerospace engineering.

From 1987 to 1990, he was a systems engineer at Hughes Space and Communications Group responsible for mission analysis on commercial and government spacecraft programs. He was a research associate at Stanford from 1996 to 1998, serving as project leader for GPS Local Area Augmentation System (LAAS) research and development. He is now a Professor of Mechanical and Aerospace Engineering at the Illinois Institute of Technology (IIT) in Chicago.

Prof. Pervan is a member of the AIAA and of the ION. He was the recipient of the Mechanical and Aerospace Dept. Excellence in Research Award (2007), IIT/Sigma Xi Excellence in University Research Award (2005), University Excellence in Teaching Award (2005), Ralph Barnett Mechanical and Aerospace Dept. Outstanding Teaching Award (2002, 2009), IEEE Aerospace and Electronic Systems Society M. Barry Carlton Award (1999), RTCA William E. Jackson Award (1996), Guggenheim Fellowship (Caltech 1987), and Albert J. Zahm Prize in Aeronautics (Notre Dame 1986). He is currently Editor of the ION journal *Navigation*.